Progress In Electromagnetics Research, Vol. 133, 443–458, 2013

DESIGN AND 3-D PARTICLE-IN-CELL SIMULATION OF A 140 GHz SPATIAL-HARMONIC MAGNETRON

N. Nasr Esfahani[1, 2, *], M. Tayarani[1], and K. Schünemann[2]

[1]Faculty of Electrical Engineering, Iran University of Science and Technology (IUST), Narmak, Tehran 1684613114, Iran

[2]Institut für Hochfrequenztechnik, Technische Universität Hamburg-Harburg, Hamburg D-21073, Germany

Abstract—This paper discusses design procedure and 3-D numerical simulation of a 140 GHz spatial-harmonic magnetron (SHM). The well known scaling laws and an approximate approach based on single harmonic analysis are used to determine the interaction space dimensions and the optimum geometrical parameters of the side resonators. Numerical simulations of the SHM were performed using CST-Particle Studio. Since the simulations are not based on artificial RF priming or assuming restrictive assumptions on the mode of operation or on the number of harmonics to be considered, electromagnetic oscillations grow naturally from noise. The presented SHM shows stable operation in the $\pi/2-1$-mode at 140 GHz over a range of DC anode voltages extending from 11.3 kV to 11.5 kV and for an axial magnetic flux density equal to 0.79 T. Output power of the SHM varies from 2 kW to 11 kW over these voltages with a maximum efficiency of about 6.8%.

1. INTRODUCTION

Recent years have seen increased interest in the Terahertz (THz) region of the electromagnetic spectrum because of a number of potential applications in industrial quality control, remote sensing, stand-off detection of chemical and biological agents, medical imaging, ultra high speed data communications, all weather visibility systems, astrophysics, and spectroscopy [1–4]. Although various components have been developed for THz applications [5–18], high power, low cost, and compact THz sources are not readily available [19]. With

Received 13 August 2012, Accepted 31 October 2012, Scheduled 1 November 2012

* Corresponding author: Nasrin Nasr Esfahani (nna@tf.uni-kiel.de).

the rapid advancement of multi-physics based codes, which provide the possibility of simulating the nonlinear beam-wave interaction dynamics [20–24], extending the operating frequency of the existing microwave tube designs [25–29] has become a promising approach for developing compact and powerful THz sources [30–36]. In accordance with this approach, design and numerical simulations of a 140 GHz spatial-harmonic magnetron (SHM) with a maximum pulse-output power of about 11 kW is presented in this paper. SHMs utilize the first backward harmonic of the $\pi/2$-mode (also called $n = N/4$-mode, where n means mode number, and N is the number of side resonators in the anode block. $2\pi n/N$ shows the phase shift between the adjacent side resonators) or of neighboring ones ($\pi/2 \pm 1$ ($n = N/4 \pm 1$)-mode) instead of the fundamental harmonic of the π-mode (also called $n = N/2$-mode), which is employed in classical magnetrons. Utilizing the first backward harmonic of the $\pi/2$ (or $\pi/2 \pm 1$)-mode in the spatial harmonic scenario helps to decrease the required DC magnetic flux density and to increase the magnetron cavity dimensions. Hence, SHMs are able to remove fundamental drawbacks of the π-mode scenario in the millimeter-wave band, i.e., the necessity of employing high magnetic flux densities and impractically small anode cavities. SHMs have much better mode separation in both frequency and phase velocity domains as compared to the π-mode magnetrons. Due to this, SHMs do not suffer from mode competition even if the anode structure is neither strapped nor of rising sun type. Another practical limitation of the π-mode scenario in the millimeter-wave band is the short life time of the thermionic cathode due to its high current density. This limitation has been successfully removed in SHMs by introducing a cold cathode instead of a thermionic one [37, 38]. The advantages of SHMs over classical magnetrons can provide the possibility of extending the operating frequency of these devices to near THz and THz frequency ranges. In the second section of the paper, design procedure and details of the simulation model of a 140 GHz SHM are presented. In this section, the effect of important geometrical parameters of the anode block on output power is determined using the results of a theory based on the single harmonic approximation approach. This enables the determination of the optimum geometrical parameters of the side resonator which maximizes the output power in a wide range of external quality factor. In Section 3, simulation results consisting of space charge profiles, output power and efficiency are presented, and the accuracy of the single harmonic approximation approach is examined. In Section 4, considerations regarding the pulse duration selection and vacuum breakdown are presented. Finally, a brief conclusion is presented in Section 5.

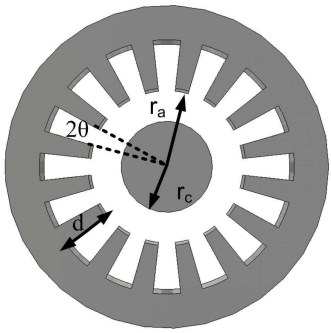

Figure 1. A cut-away view of the anode block of an SHM together with a concentric cathode.

2. DESIGN PROCEDURE AND SIMULATION MODEL

SHMs employ the conventional anode structure of the classical π-mode magnetrons, i.e., a coaxial cylindrical cavity loaded with identical side resonators (Fig. 1). The geometrical parameters of the SHM cavity (Fig. 1) are: cathode radius r_c, anode radius r_a, number of side resonators N, resonator depth d, and resonator opening θ. In our simulation model, the geometrical parameters of the interaction space and the number of side resonators, i.e., r_a, r_c, and N are 1.3 mm, 0.7 mm, and 28 respectively. Based on the well known scaling laws [39], these geometrical parameters have been determined from the corresponding parameters of a 28 cavity, 95 GHz ($\pi/2-1$-mode) SHM [37]. These dimensions are also close to that of a tunable 2 mm-wavelength-band SHM [38]. As will be presented in the next subsection, θ and d are selected in a way that they can provide maximum output power for the $\pi/2-1$-mode with a resonant frequency of about 140 GHz.

2.1. Optimum Geometry of the Side Resonators

Considering the single harmonic approximation approach [39], output power of an SHM can be formulated as follows [40]:

$$P_{Out} = \frac{Q_{ext}}{\left(1+\frac{Q_{ext}}{Q_u}\right)^2}\frac{A_{-1}^2 I^2}{\pi F f_n} \tag{1}$$

where A_{-1} means the amplitude of the synchronous harmonic (first backward harmonic) of the electric field of the operating mode ($\pi/2-1$-mode) which is calculated using (2) [39]. I depends on the current

density and the field distribution in the interaction space and on the operating mode, but weakly depends on the geometrical parameters of the side resonators as long as the resonant frequency does not vary considerably [40]. Q_u means the unloaded quality factor, Q_{ext} means external quality factor, f_n is the resonant frequency of the operating mode, and F is a form factor which is determined using (3) [41].

$$A_{-1} = \frac{4}{3\pi} \sin\left(\frac{3N}{4}\theta\right) \tag{2}$$

$$F = \frac{2U}{C_n^2} \tag{3}$$

where U means the RF energy stored per unit length of the SHM cavity and C_n is the amplitude of the electric field in the interaction space. By solving Maxwell's equations in the interaction space and side resonators and satisfying the boundary conditions at the interface between the side resonators and the interaction space, f_n, F, and Q_u have been calculated. Based on these calculations, the effect of the geometrical parameters on P_{Out} can be determined using (1). Since here we are interested in having the anode and cathode radii close to the previously mentioned values and also in having a constant resonant frequency of about 140 GHz, we vary the values of d and θ simultaneously. The dependence of the normalized values of P_{Out}/I^2 on the normalized aperture opening ($N\theta/\pi$) for different values of Q_{ext} is shown in Fig. 2. For each value of $N\theta/\pi$, d is selected in a way that provides $f_n = 140$ GHz. Normalized value of the aperture opening for the designed SHM is selected to be 0.55 which corresponds to the maximum value of the normalized P_{Out}/I^2 (Fig. 2). Table 1 summarizes the important characteristics of the designed SHM.

Table 1. Geometrical parameters, operating and neighboring modes and their resonant frequencies for the designed SHM.

Cathode radius (r_c)	0.7 mm
Anode radius (r_a)	1.3 mm
Anode length	1.5 mm
$N\theta/\pi$	0.55
Side resonator depth (d)	0.354 mm
Number of side resonators (N)	28
$5(\pi/2-2)$-mode resonant frequency	131.4 GHz
$6(\pi/2-1)$-mode resonant frequency	140 GHz
$7(\pi/2)$-mode resonant frequency	146.6 GHz

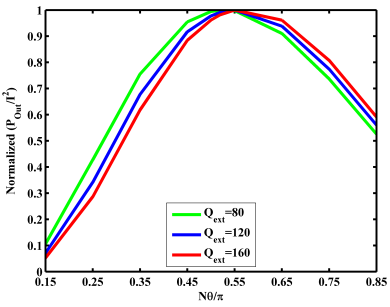

Figure 2. Normalized values of P_{Out}/I^2 versus $N\theta/\pi$ for Q_{ext} varying from 80 to 160.

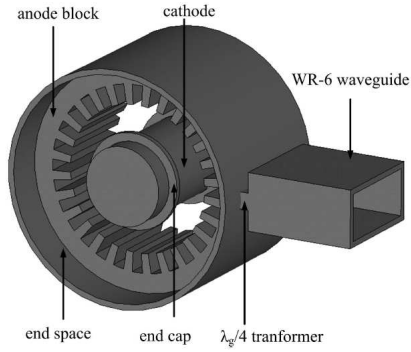

Figure 3. Simulation model of the SHM.

2.2. Simulation Model in CST-particle Studio

The simulation model of the SHM consists of an anode block with 28 side resonators, an impedance matching section (a $\lambda_g/4$ transformer), an output waveguide (WR6), and a cold secondary-emission cathode with two nonmagnetic end caps, which provide uniform magnetic field, and confine the electron cloud in the interaction region (Fig. 3). The total current in the SHMs is mainly due to secondary emission from a cold cathode, which is typically made of a copper core coated with a platinum foil [37, 38]. In the SHMs, these cathodes are initialized by a bombarding current provided by an auxiliary thermionic cathode placed outside of the interaction space. An exact incorporation of the auxiliary cathode in the simulation model is complicated, and it is only required for initializing the secondary-emission cathode [40], hence similar to [40, 42], our model does not incorporate the exact modeling of the auxiliary cathode. In our simulations, the initialized bombarding current which is a small amount of the total current in the SHMs, is provided by specifying a relatively small primary emission current ($I_p = 12\,\mathrm{A}$) to the cold cathode. This primary emission is sufficient to initiate the emission of secondary electrons. Due to the main contribution of secondary emission, accurate modeling of this phenomenon is of principal importance for any SHM simulation. The average number of the emitted secondary electrons from the cold cathode, which depends on the impact energy (ω_0) and impact angle (α) of the primary electrons, is called secondary emission yield ($\delta(\omega_0, \alpha)$). For normal incidence angle, the maximum of secondary emission yield for platinum (Fig. 4) is found as 1.8 [42] which is

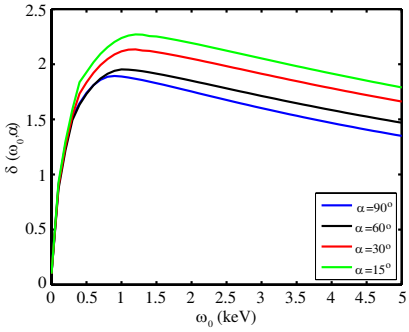

Figure 4. Secondary emission yield for platinum versus impact energy for different incidence angles.

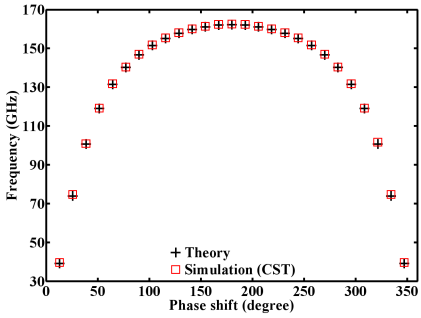

Figure 5. Analytically calculated and simulated (using CST) resonant frequencies as a function of the phase shift between two adjacent side resonators.

sufficient to initiate an avalanche process in the growth of the electron concentration in the interaction space by utilizing a small bombarding current.

For SHMs as for other pulsed magnetrons, the radial electric field between the cathode and anode is produced by a pulsed power device. However, the simulation model presented here does not include details of circuit and switches of the pulsed power device. This approach is typical for 3-D PIC simulations of magnetron oscillators [43, 44].

3. SIMULATION RESULTS

Figure 5 shows the resonant frequencies as a function of the phase shift between two adjacent side resonators for two cases: analytically calculated resonant frequencies assuming perfect magnetic conductor (PMC) walls at the top and bottom of the anode block and neglecting the end-space geometry and end caps; and simulated resonant frequencies (using CST) obtained from a realistic model (Fig. 3). The slight discrepancy between the realistic model simulation results and the results based on the PMC wall assumption is due to the effects of the end caps, end spaces, quarter-wavelength transformer, and output waveguide in the realistic model. Resonant modes are identified from the vector electric field profile at each resonant frequency. The operating $\pi/2-1$-mode (also called $n = 6$-mode), for which the phase shift between the adjacent side resonators is $77.14°$, is found to be resonant at 140 GHz. In contrast to the resonant frequency of the π-

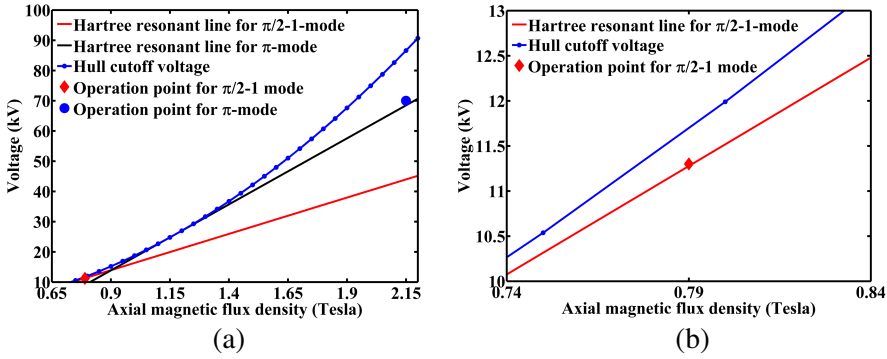

Figure 6. (a) Hull cutoff parabola, Hartree resonant condition, and the operating points for the π-mode and the $\pi/2-1$-mode. (b) Hull cutoff parabola, Hartree resonant condition for $\pi/2-1$-mode around the operating point of this mode.

mode, the resonant frequency of the operating mode is well separated from its neighboring modes (Fig. 5). This is one of the advantages of the non-π-mode operation. One may plot the Hull cutoff parabola, the Hartree resonant line of the π- and $\pi/2-1$-modes, one of the examined operating points of the SHM ($V_{DC} = 11.3\,\text{kV}$ and $B = 0.79\,\text{T}$), and a typical operating point for π-mode to confirm the importance of employing the spatial harmonic operation in reducing the required V_{DC} and B values (Fig. 6(a)). The operating point of SHM is usually selected in the region where the Hartree resonant line and the Hull cutoff parabola are close to each other (Fig. 6(b)). This trend is consistent with the theoretical expectations, because, as was mentioned before, the wave-particle interaction in the SHM is realized as an interaction of electrons with the first backward harmonic of the $\pi/2$ (or $\pi/2\pm1$)-mode, and this harmonic is localized near the anode structure so that, in order to realize an effective electron-wave interaction, the value of V_{DC} should be close to its critical value determined by the Hull cutoff parabola.

The nonlinear beam-wave interaction dynamics are examined through the use of a PIC simulator embedded in CST-Particle Studio. The presented simulations do not suffer from restrictive assumptions on the number of modes or on the number of spatial harmonics, which are among common restrictions in the numerical simulation methods based on the mode expansion technique [40, 42]. While studying the time evolution of the space charge in the interaction space, the electron cloud initially forms in the area near the emission points assumed

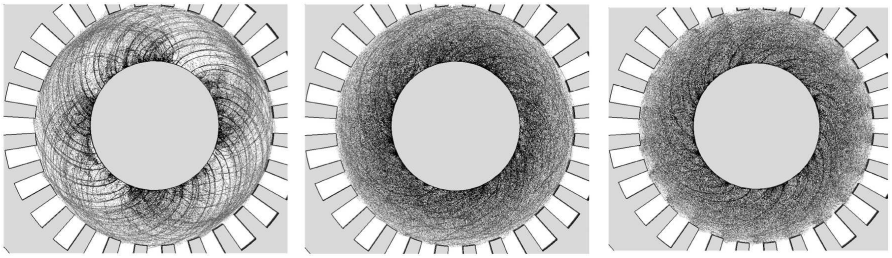

Figure 7. Time-evolved spoke formation plotted in the $r\theta$ plane at (a) 0.4 ns, (b) 1.4 ns, and (c) 5 ns. The results are for $V_{DC} = 11.3\,\mathrm{kV}$, $B = 0.79\,\mathrm{T}$, and $Q_{ext} = 160$.

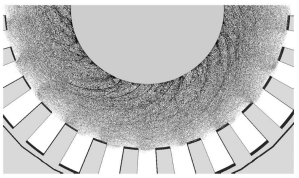

Figure 8. Zoomed view of Fig. 7(c).

on the cathode and then expands until it fills the whole interaction space (Fig. 7). As time elapses, 22 electron bunches appear near the anode surface (Fig. 7(c)). The presence of the electron bunches is easily realizable in Fig. 8, which shows the electron bunches near the anode surface in a half of the interaction space. As is known, the number of spokes is equal to the number of complete periods γ (where $\gamma = mN+n$, m and n mean harmonic and mode number, respectively) of the synchronous harmonic around the anode circumference. Thus, formation of 22 electron bunches indicates the synchronism between the first backward harmonic ($m = -1$) of the $\pi/2$ − 1-mode ($n = 6$-mode) and the space-charge and this confirms the $\pi/2$ − 1-mode oscillations. Beyond 5 ns, this mode is dominant for the whole duration of the simulation. Output voltage starts to grow abruptly at about 3 ns and reaches its saturation value ($V_{Out} = 1470\,\mathrm{V}$) after 5 ns (Fig. 9). The saturated output power is calculated using

$$P_{Out} = (a/4bZ_0)\, V_{Out}^2 \sqrt{\left(1 - (f_c/f)^2\right)}$$

where a and b are the output waveguide width and height, respectively, and Z_0, f_c, and f mean wave impedance, cutoff frequency of output waveguide (WR6), and the operating frequency. Considering a =

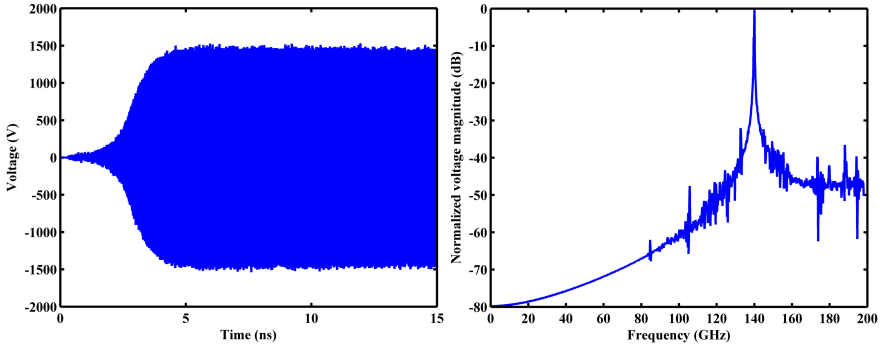

Figure 9. (a) Output voltage amplitude measured at the centerline of the output port across the output waveguide broad walls. (b) Normalized amplitude of the frequency spectrum obtained from a Fourier transform of the time-varying output voltage. The results are for $V_{DC} = 11.3\,\text{kV}$, $B = 0.79\,\text{T}$, and $Q_{ext} = 160$.

1.651 mm, $b = 0.8255\,\text{mm}$, and $V_{Out} = 1470$ V, the saturated output power is equal to 2.18 kW. Simulation results show that after 5 ns a nearly constant current of about 6.8 A is collected on the anode ($I_{Anode} = 6.8\,\text{A}$). Considering the previously mentioned values for anode current, DC-anode voltage, saturated output power, and the input power which is given by $P_{in} = I_{Anode}V_{DC}$, the efficiency is 2.83%.

PIC simulations have also been carried through for other 28-resonator, 140 GHz ($n = 6$-mode) SHMs with the values of $N\theta/\pi$ ranging from 0.25 to 0.75 and with the interaction space dimensions provided in Table 1. As can be seen in Fig. 10, maximum of output power appears at around $N\theta/\pi = 0.55$ which is in accordance with the $N\theta/\pi$ related to the maximum of the normalized values of P_{Out}/I^2 (Fig. 2) calculated based on the single harmonic approximation approach. Hence, it can be concluded that the single harmonic approximation approach, which only depends on the geometrical parameters of the SHM cavity, can be employed to determine the optimum value of θ.

4. CONSIDERATIONS REGARDING THE PULSE DURATION SELECTION AND VACUUM BREAKDOWN

Surface temperature of copper T, which depends on the dissipated power on the anode block P_a, pulse duration τ, and the anode surface

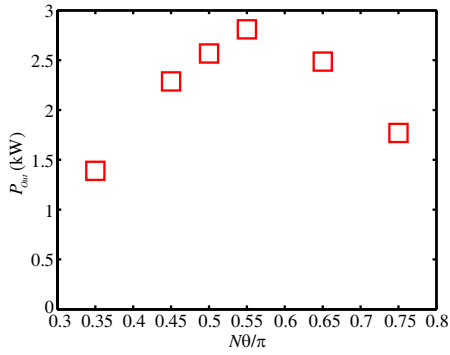

Figure 10. Dependency of P_{Out} on $N\theta/\pi$ for $V_{DC} = 11.3\,\text{kV}$, $B = 0.79\,\text{T}$, and $Q_{ext} = 160$.

area S_a, can be determined using [45]

$$T = \frac{0.3 P_a \sqrt{\tau}}{10000 S_a} \tag{4}$$

According to the safety rules, the copper surface temperature should not exceed 110°C. For $V_{DC} = 11.3\,\text{kV}$ and $B = 0.79\,\text{T}$, the dissipated power at the anode block of the designed SHM is about 60 kW. Using (4) and considering $P_a = 60\,\text{kW}$, it can be concluded that the pulse duration should be less than about 170 ns. On the other hand, the vane tips of the designed SHM are only 0.16 mm apart (Section 2) and with this degree of separation vacuum breakdown that can occur due to the high RF field between vanes may impede the operation of this SHM. A threshold value for the electric field and voltage at which breakdown may be expected to occur depends on the pulse duration τ and can be determined using [46]:

$$E_t < 8000/V_t \tag{5}$$

for long pulses ($\tau \geq 1\,\text{ms}$), and

$$E_t < 1000/V_t \tau^{0.34} \tag{6}$$

for short pulses ($\tau \leq 1\,\text{ms}$). Here V_t is voltage in kV, E_t is the electric field magnitude in kV/cm, and τ is the pulse duration in s. At the resonator opening, the electric field which is nearly uniform can be calculated using

$$E_{ap} = V/2r_a\theta \tag{7}$$

where V is the voltage amplitude at the aperture opening, and r_a and θ are the anode radius and resonator opening (Fig. 1), respectively.

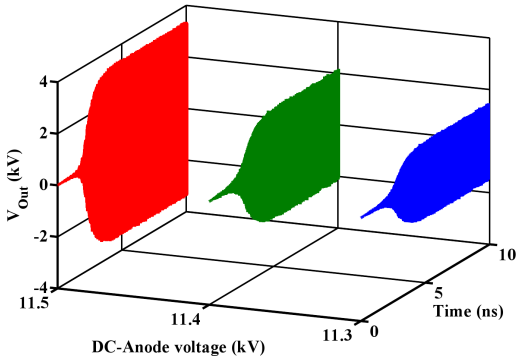

Figure 11. Output voltage for $B = 0.79$ T, $Q_{ext} = 160$, and for V_{DC} varying from 11.3 kV to 11.5 kV.

Table 2. Important features of the designed SHM for the whole variation range of V_{DC}.

V_{DC} (kV)	P_a (kW)	Efficiency %	Pulse duration (ns)	E_{ap} (kV/cm)	E_t (kV/cm)
11.5	11	6.8	30	219	4800
11.4	4.5	4.3	60	133	4200
11.3	2.18	2.83	100	93	3800

Using (6) and (7) and considering $\tau = 100$ ns, the electric field magnitude threshold for the designed SHM is equal to 3800 kV/cm. Simulations show that for an output power of 2.18 kW, the electric field magnitude at the resonator opening is 93 kV/cm. This value is far below the threshold. Thus, $\tau = 100$ ns ensures the safe operation of the SHM from both thermal and vacuum breakdown analysis point of view. The designed SHM also shows stable operation for $V_{DC} = 11.4$ kV and $V_{DC} = 11.5$ kV (Fig. 11). While varying V_{DC} from 11.3 kV to 11.5 kV, maximum efficiency and output power of the designed SHM are 6.8% and 11 kW, respectively (Table 2). In this case, the pulse duration should not exceed 30 ns.

5. CONCLUSIONS

In this paper, design and 3-D simulations of a 140 GHz SHM using CST-Particle Studio have been presented. Based on a single harmonic approximation approach, the effect of the aperture opening on the

output power has been examined, and an optimum value for the aperture opening has been determined. PIC simulation results confirm the accuracy of the approximate approach in predicting an optimum value for the aperture opening. The designed SHM shows a stable operation for DC-anode voltages ranging from 11.3 kV to 11.5 kV. For these voltages, the electric field at the aperture opening does not exceed the threshold value of the electric field corresponding to vacuum breakdown. Based on thermal considerations, appropriate values for the pulse duration have been determined. Output power and efficiency of the designed SHM vary from 2 kW to 11 kW and from 2.8% to 6.8%, respectively.

REFERENCES

1. Booske, J., R. Dobbs, C. Joy, C. Kory, G. Neil, G. Park, J. Park, and R. Temkin, "Vaccum electronic high power terahertz sources," *IEEE Trans. Terahertz Sci. Tech.*, Vol. 1, No. 1, 54–75, 2011.
2. Heh, D. Y. and E. L. Tan, "Modeling the interaction of terahertz pulse with healthy skin and basal cell carcinoma using the unconditionally stable fundamental adi-FDTD method," *Progress In Electromagnetics Research B*, Vol. 37, 365–386, 2012.
3. Kuznetsov, S. A., A. G. Paulish, A. V. Gelfand, P. A. Lazorskiy, and V. N. Fedorinin, "Matrix structure of metamaterial absorbers for multispectral terahertz imaging," *Progress In Electromagnetics Research*, Vol. 122, 93–103, 2012.
4. Cai, M. and E. P. Li, "A novel terahertz sensing device comprising of a parabolic reflective surface and a bi-conical structure," *Progress In Electromagnetics Research*, Vol. 97, 61–73, 2009.
5. Zhang, Y.-X., S. Qiao, T. Zhao, W. Ling, and S. Liu, "Planar symmetric normal and complementary three-resonance resonators in terahertz band," *Progress In Electromagnetics Research*, Vol. 125, 21–35, 2012.
6. Sabah, C. and H. G. Roskos, "Design of a terahertz polarization rotator based on a periodic sequence of chiral-metamaterial and dielectric slabs," *Progress In Electromagnetics Research*, Vol. 124, 301–314, 2012.
7. Zhou, H., F. Ding, Y. Jin, and S. He, "Terahertz metamaterial modulators based on absorption," *Progress In Electromagnetics Research*, Vol. 119, 449–460, 2011.
8. He, X.-J., Y. Wang, J. Wang, T. Gui, and Q. Wu, "Dual-band terahertz metamaterial absorber with polarization insensitivity

and wide incident angle," *Progress In Electromagnetics Research*, Vol. 115, 381–397, 2011.

9. Andres-Garcia, B., L. E. Garcia-Munoz, D. Segovia-Vargas, I. Camara-Mayorga, and R. Gusten, "Ultrawideband antenna excited by a photomixer for terahertz band," *Progress In Electromagnetics Research*, Vol. 114, 1–15, 2011.
10. Zhou, Y. and S. Lucyszyn, "Modelling of reconfigurable terahertz integrated architecture (Retina) SIW structures," *Progress In Electromagnetics Research*, Vol. 105, 71–92, 2010.
11. Laurette, S., A. Treizebre, N.-E. Bourzgui, and B. Bocquet, "Terahertz interferometer for integrated Goubau-line waveguides," *Progress In Electromagnetics Research Letters*, Vol. 30, 49–58, 2012.
12. Diao, J., F. Yang, L. Du, J. Ou Yang, and P. Yang, "Enhancing terahertz radiation from dipole photoconductive antenna by blending tips," *Progress In Electromagnetics Research Letters*, Vol. 25, 127–134, 2011.
13. Gu, C., S. Qu, Z. Pei, H. Zhou, J. Wang, B.-Q. Lin, Z. Xu, P. Bai, and W.-D. Peng, "A wide-band, polarization-insensitive and wide-angle terahertz metamaterial absorber," *Progress In Electromagnetics Research Letters*, Vol. 17, 171–179, 2010.
14. Diao, J. M., F. Yang, Z.-P. Nie, J. Ou Yang, and P. Yang, "Separated fractal antennas for improved emission performance of terahertz radiations," *Journal of Electromagnetic Waves and Applications*, Vol. 26, No. 8–9, 1158–1167, 2012.
15. Diao, J. M., L. Du, J. Ou Yang, P. Yang, and Z.-P. Nie, "Enhanced center frequency of terahertz pulse emission from photoconductive antenna," *Journal of Electromagnetic Waves and Applications*, Vol. 25, No. 16, 2236–2243, 2011.
16. Gao, Z. and Z.-Y. Wang, "Terahertz plasmonic cross resonant optical antenna," *Journal of Electromagnetic Waves and Applications*, Vol. 25, No. 11–12, 1730–1739, 2011.
17. Zhang, X. F., L. F. Shen, J.-J. Wu, and T.-J. Yang, "Backward guiding of terahertz radiation in periodic dielectric waveguides," *Journal of Electromagnetic Waves and Applications*, Vol. 24, No. 4, 557–564, 2010.
18. Chen, D. and H. Chen, "Highly birefringent low-loss terahertz waveguide: Elliptical polymer tube," *Journal of Electromagnetic Waves and Applications*, Vol. 24, No. 11–12, 1553–1562, 2010.
19. Nguyen, T. K., T. A. Ho, I. Park, and H. Han, "Full-wavelength dipole antenna on a gaas membrane covered by a

frequency selective surface for a terahertz photomixer," *Progress In Electromagnetics Research*, Vol. 131, 441–455, 2012.

20. Ding, S., B.-F. Jia, F.-X. Li, and Z.-J. Zhu, "3D Simulation of 18-vane 5.8 GHz Magnetron," *Journal of Electromagnetic Waves and Applications*, Vol. 22, Nos. 14–15, 1925–1930, 2008.
21. Ashutosh, B., R. Chandra, and P. K. Jain, "Multimode behavior of a 42 GHz, 200 kW gyrotron," *Progress In Electromagnetics Research B*, Vol. 42, 75–91, 2012.
22. Singh, U., N. Kumar, S. Tandon, H. Khatun, L. P. Purohit, and A. K. Sinha, "Numerical simulation of magnetron injection gun for 1 mw 120 GHz gyrotron," *Progress In Electromagnetics Research Letters*, Vol. 16, 21–34, 2010.
23. Jain, R. and M. V. Kartikeyan, "Design of a 60 GHz, 100 kw cw gyrotron for plasma diagnostics: Gds-v.01 simulations," *Progress In Electromagnetics Research B*, Vol. 22, 379–399, 2010.
24. Kumar, N., U. Singh, A. Kumar, H. Khatun, T. P. Singh, and A. K. Sinha, "Design of 35 GHz gyrotron for material processing applications," *Progress In Electromagnetics Research B*, Vol. 27, 273–288, 2011.
25. Kesari, V., "Beam-absent analysis of disc-loaded-coaxial waveguide for application in Gyro-TWT (part-1)," *Progress In Electromagnetics Research*, Vol. 109, 211–227, 2010.
26. Kesari, V., "Beam-present analysis of disc-loaded-coaxial waveguide for its application in Gyro-TWT (part-2)," *Progress In Electromagnetics Research*, Vol. 109, 229–243, 2010.
27. Hou, Y., J. Xu, H.-R. Yin, Y.-Y. Wei, L.-N. Yue, G. Zhao, and Y.-B. Gong, "Equivalent circuit analysis of ridge-loaded folded-waveguide slow-wave structures for millimeter-wave traveling-wave tubes," *Progress In Electromagnetics Research*, Vol. 129, 215–229, 2012.
28. Liu, Y., J. Xu, Y.-Y. Wei, X. Xu, F. Shen, M. Huang, T. Tang, W.-X. Wang, and Y.-B. Gong, "Design of a V-band high-power sheet-beam coupled-cavity traveling-wave tube," *Progress In Electromagnetics Research*, Vol. 123, 31–45, 2012.
29. Seshadri, R., S. K. Ghosh, A. Bhansiwal, S. Kamath, and P. K. Jain, "A simple analysis of helical slow-wave structure loaded by dielectric embedded metal segments for wideband traveling-wave tubes," *Progress In Electromagnetics Research B*, Vol. 20, 303–320, 2010.
30. Zheng, R., P. Ohlckers, and X. Chen, "Particle-in-cell simulation and optimization for a 220 GHz folded waveguide traveling wave

tube," *IEEE Trans. Electron Devices*, Vol. 58, No. 7, 2164–2171, 2011.

31. Gensheimer, P. D., C. K. Walker, R. W. Ziolkowski, and C. D. Aubigny, "Full-scale three-dimensional simulations of a folded-waveguide traveling-wave tube using ICEPIC," *IEEE Trans. Terahertz Sci. Tech.*, Vol. 2, No. 3, 222–230, 2011.
32. Gong, Y., H. Yin, L. Yue, Z. Lu, Y. Wei, J. Feng, Z. Duan, and X. Xu, "A 140 GHz two beam over moded folded-waveguide traveling-wave tube," *IEEE Trans. Terahertz Sci. Tech.*, Vol. 39, No. 3, 847–851, 2011.
33. Mineo, M. and C. Paoloni, "Corrugated rectangular waveguide tunable backward wave oscillator for THz applications," *IEEE Trans. Plasma Sci.*, Vol. 57, No. 5, 1481–1484, 2010.
34. Xu, X., Y. Wei, F. Shen, Z. Duan, Y. Gong, H. Yin, and W. Wang, "Sine waveguide for 0.22 THz traveling wave tube," *IEEE Electron Device Letters*, Vol. 32, No. 8, 1152–1153, 2011.
35. Xu, X., Y. Wei, F. Shen, Z. Duan, Y. Gong, H. Yin, and W. Wang, "140 GHz V-shaped microstrip meander-line traveling wave tube," *Journal of Electromagnetic Waves and Applications*, Vol. 32, No. 8, 1152–1153, 2011.
36. Zhang, M. H, Y.-Y. Wei, G. Guo, L. -N. Yue, Y. Hou, S. M. Wang, J. Xu, Y.-B. Gong, and W.-X. Wang, "A novel 140-GHz sheet-beam folded-waveguide traveling-wave tube," *Journal of Electromagnetic Waves and Applications*, Vol. 26, Nos. 17–18, 1–9, 2012.
37. Naumenko, V. D., K. Schünemann, and D. M. Vavriv, "Miniature 1 kW, 95 GHz magnetrons," *Electronics Letters*, Vol. 35, No. 22, 1960–1961, 1998.
38. Naumenko, V. D., A. Suvorov, and A. Sirov, "Tunable magnetron of a two-millimeter-wavelength band," *Microwave and Optical Technology Letters*, Vol. 12, No. 3, 129–131, 1996.
39. Collins, G. B., *Microwave Magnetrons*, McGrow-Hill, New York, 1948.
40. Schünemann, K., A. E. Serebryannikov, S. V. Sosnytskiy, and D. M. Vavriv, "Optimizing the spatial-harmonic millimeter-wave magnetron," *Physics of Plasmas*, Vol. 10, No. 6, 2559–2565, 2003.
41. Yu, S., G. Kooyers, and O. Bunemann, "Time dependent computer analysis of electron-wave interaction in crossed fields," *Journal of Appl. Phys.*, Vol. 36, No. 8, 2550–2559, 1965.
42. Schünemann, K., S. V. Sosnytskiy, and D. M. Vavriv, "Self-consistent simulation of the spatial-harmonic magnetron with

cold secondary-emission cathode," *IEEE Trans. Electron Devices*, Vol. 48, No. 5, 993–998, 2001.

43. Andreev, A. D. and K. J. Hendricks, "ICEPIC simulation of a strapped nonrelativistic high-power CW UHF magnetron with a solid cathode operating in the space-charge limited regime," *IEEE Trans. Plasma Sci.*, Vol. 40, No. 6, 1551–1562, 2012.
44. Fleming, T. P., M. Lambrecht, and P. Mardahl, "Design and simulation of a Mega-watt class non relativistic magnetron," *IEEE Trans. Plasma Sci.*, Vol. 40, No. 6, 1563–1568, 2012.
45. Kovalenko, V. F., *Physics of Heat Transfer and Electro-vacuum Devices*, Soviet Radio, Moscow, 1975.
46. Latham, R. V., *High Voltage Vacuum Insulation*, Academic Press, London, 1995.